

Continuous Wigner-Mott transition at $\nu = 1/5$

Thomas G. Kiely and Debanjan Chowdhury

Department of Physics, Cornell University, Ithaca, New York 14853, USA.

Electrons can organize themselves into charge-ordered states to minimize the effects of long-ranged Coulomb interactions. In the presence of a lattice, commensurability constraints lead to the emergence of incompressible Wigner-Mott (WM) insulators at various rational electron fillings, $\nu = p/q$. The mechanism for quantum fluctuation-mediated melting of the WM insulators with increasing electron kinetic energy remains an outstanding problem. Here we analyze numerically the bandwidth-tuned transition out of the WM insulator at $\nu = 1/5$ on infinite cylinders with varying circumference. For the two-leg ladder, the transition from the WM insulator to the Luttinger liquid proceeds via a distinct intermediate phase with gapless Cooper-pairs and gapped electronic excitations. The resulting Luther-Emery liquid is the analog of a strongly fluctuating superconductor. We place these results in the context of a low-energy bosonization based theory for the transition. On the five-leg cylinder, we provide numerical evidence for a direct continuous transition between the WM insulator and a metallic phase across which the spin and charge-gaps vanish simultaneously. We comment on the connections to ongoing experiments in dual-gated bilayer moiré transition metal dichalcogenide materials.

Introduction.- The emergence of Wigner-Mott (WM) insulators¹ at a partial commensurate filling of electronic bands is one of the hallmarks of an interaction-induced phenomenon [1]. Despite being an old problem, much remains to be understood about how a WM insulator emerges from a Landau-Fermi liquid (FL) at a fixed electronic filling (ν) as a function of increasing strength of interactions. The FL metal hosts an electronic Fermi surface whose area is fixed by Luttinger's theorem [2, 3]. On the other hand, the WM insulator does *not* host any electronic Fermi surface and spontaneously breaks space-group (and, possibly, spin-rotation) symmetries. Given these differences, one might expect that the most common scenario would be for the metal-insulator transition to be first-order in nature, which is seen in many solid-state materials [4]. An alternative “weak-coupling” perspective suggests that the transition can proceed via intermediate metallic phases with broken translational symmetry and an even number of electrons in the enlarged unit-cell. Examples of both classes of transitions, including the additional effects of disorder, have been analyzed in a large body of earlier work [5–8]. The most intriguing scenario involves a direct continuous transition between a symmetry-preserving FL metal and a WM insulator. As a matter of principle, such continuous transitions can be described using quantum field theoretic methods involving fractionalized degrees of freedom and emergent gauge-fields [9, 10], but they typically rely on artificial limits to make computational progress.

In this letter, we study the transition(s) between a WM insulator and a FL metal at a fixed filling $\nu = 1/5$ for spinful electrons on the triangular lattice using infinite matrix product state (MPS) techniques [11, 12]. In the strong-coupling regime, superexchange leads to a spin-

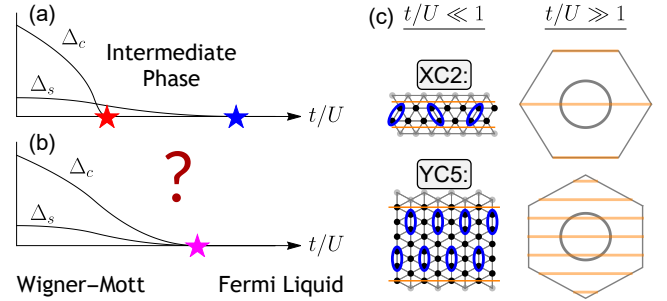


FIG. 1. Schematic for two possible scenarios for continuous bandwidth-tuned WM transitions at $\nu = 1/5$, where Δ_c , Δ_s vanish at: (a) two separate QCP, with an intermediate gapless phase, or (b) the same QCP but with distinct critical exponents. (c) The two quasi-2D infinite cylinder geometries, XC2 and YC5, along with the respective WM insulators ($t/U \ll 1$) and the electronic Fermi surface in the metallic phase ($t/U \gg 1$). The blue ovals denote singlet bonds and the orange lines denote cuts through the electronic Fermi surface, corresponding to the allowed momentum modes around the cylinder circumference.

singlet WM insulating ground state with finite spin and charge gaps, Δ_s , Δ_c , respectively; see Fig. 1. Starting with the fully-gapped WM insulator, which can be efficiently represented using MPS, we address the quantum fluctuation-induced melting of the WM insulator with increasing single-electron bandwidth. In particular, are there intermediate gapless phases distinct from a symmetry-preserving FL metal (Fig. 1a), or is there a direct transition to the FL across which Δ_s , Δ_c vanish simultaneously (Fig. 1b)?

With increasing quantum fluctuations, the spin-singlets in the WM insulator can melt into delocalized, but strongly fluctuating Cooper-pairs before breaking apart to reveal the electronic excitations. For a particular set of microscopic interaction parameters, we find

¹ These are also referred to as “generalized” Wigner crystals.

compelling evidence for this two-step transition on two-leg ladders where the intervening Luther-Emery liquid [13, 14] hosts a gap to single-electron excitations, but not to the spin-singlet Cooper pairs. We emphasize that this is a “strong-coupling” route to engineering superconductivity in a model with purely repulsive interactions, without the need for any microscopic attraction, by melting a crystal of localized Cooper-pairs.

On the five-leg cylinder and for a similar choice of parameters, we find evidence for a direct continuous transition between the WM insulator with broken translational symmetry and a gapless metallic phase — seemingly at odds with any Landau-Ginzburg-Wilson-based paradigm for continuous quantum phase transitions. This is corroborated in part by a non-trivial scaling collapse associated with the extracted spin and charge “gaps”, respectively.

Experimental motivation.— Bilayers of transition metal dichalcogenides (TMDs), which realize an effective moiré triangular lattice, have presented experimental evidence for a bandwidth-tuned continuous metal-Mott insulator transition at $\nu = 1/2$ [15, 16]. In parallel, a number of experiments using moiré TMDs have reported evidence for a plethora of WM insulators at electron fillings $\nu = 1/6, 1/5, 1/4$ etc., induced by the screened long-range Coulomb interactions [17–19]. Wigner crystals in the absence of a moiré potential have been reported across different platforms in earlier work [20–24]. While the nature of the electron spin-configuration, and its possible ordering, is presently unclear for all of these WM insulators, the charge-order for $\nu = 1/6$ has been imaged directly [25]. The competing spin-exchange interactions in a Wigner crystal are highly frustrated and the ordering (or lack thereof) is a delicate question, with a long theoretical history; see Refs. [26–28]. In the context of moiré systems, previous theoretical effort has focused on the crystalline regime deep in the WM insulator [29, 30]; Hartree-Fock [31–33], classical Monte-Carlo [34], and DMRG-based [35] methods have also been used to study the competition between spin and charge-orderings over a range of coupling strength and density. Momentum-space-based exact diagonalization methods have also been employed to study the metal-insulator transition for a host of other fillings [36, 37]. The WM insulator² at $\nu = 1/5$ provides a useful starting point to study the onset of electron delocalization and melting of the spin-gap, going beyond any Hartree-Fock or classical Monte-Carlo-based approach.

Model & Method.— We study the ground state phase diagram of the extended Hubbard model on the triangular

lattice, given by

$$H = H_{\text{kin}} + H_{\text{int}}, \quad (1a)$$

$$H_{\text{kin}} = -t \sum_{\langle \mathbf{r}, \mathbf{r}' \rangle, \sigma} \left(c_{\mathbf{r}\sigma}^\dagger c_{\mathbf{r}'\sigma} + \text{H.c.} \right) - \mu \sum_{\mathbf{r}} n_{\mathbf{r}}, \quad (1b)$$

$$H_{\text{int}} = U \sum_{\mathbf{r}} n_{\mathbf{r}\uparrow} n_{\mathbf{r}\downarrow} + \frac{1}{2} \sum_{\mathbf{r} \neq \mathbf{r}'} V(\mathbf{r} - \mathbf{r}') n_{\mathbf{r}} n_{\mathbf{r}'}. \quad (1c)$$

Here the electron creation and annihilation operators at site \mathbf{r} with spin σ are denoted $c_{\mathbf{r}\sigma}^\dagger, c_{\mathbf{r}\sigma}$, respectively. The on-site interaction, U , and further neighbor interactions, $V(\mathbf{r})$, are kept fixed, with the latter determined by the screened Coulomb interaction in bilayer TMD experiments [15–17]. For our calculations, we truncate $V(\mathbf{r})$ at fourth-nearest-neighbor interactions on the triangular lattice with $V_2/V_1 \approx 0.512$, $V_3/V_1 \approx 0.423$, and $V_4/V_1 \approx 0.284$, where V_n is the n^{th} nearest-neighbor interaction strength [38]. We choose $V_1/U = 0.5$. The single electron hopping is t , and the chemical potential, μ , couples to the total electron density with $n_{\mathbf{r}} = \sum_{\sigma} c_{\mathbf{r}\sigma}^\dagger c_{\mathbf{r}\sigma}$. In the remainder of this manuscript, we focus on the electron filling fraction $\nu = 1/5$ and in the zero-magnetization sector. The phase diagram is then studied by varying t at fixed filling and interaction.

We make use of infinite matrix product state (iMPS) techniques on two quasi-2D geometries: the two-leg ladder (XC2) and the five-leg cylinder (YC5). These are shown schematically in Fig. 1(c). Using the VUMPS algorithm [39], we find the variationally-optimal iMPS approximation to the ground state for a range of bond dimensions, χ [11, 12]. In order to deduce the properties of gapless phases, we utilize finite-entanglement scaling [40, 41]. This is in some sense analogous to finite-length scaling at a critical point, where the relevant length scale is the correlation length ξ_{iMPS} . By studying how various measurable properties change as a function of ξ_{iMPS} , one can deduce the properties of the ground state wavefunction [38]. In this way, we determine the ground state properties by carefully extrapolating $\chi \rightarrow \infty$ [38]. For the XC2 geometry, we perform VUMPS simulations with bond dimensions $100 \leq \chi \leq 800$. For the YC5 geometry, we use bond dimensions $\chi = 400, 800, 1200, 1600$ and 2400 , respectively.

Two-leg ladders.— We perform calculations with the XC2 geometry for two different choices of the hopping parameters. We denote the hopping amplitude along the short direction t and the amplitude along the long direction t' (see Fig. 1). For (a) $t = t'$, the bandstructure leads to 2 Fermi points (FP), as in Fig. 2a, while for (b) $t = 6t'$ there are 4 FP as in Fig. 2f. Let us denote the metallic phase in the corresponding bosonized model as $C\alpha S\beta$, where α (β) denote the number of charge (spin) modes, respectively. For both cases, we find a WM insulator on the two-leg ladder for $U/t \gg 1$ and a metallic Luttinger liquid (LL) for $U/t \ll 1$ (see Fig. 1c). However, we do *not* find a direct transition between these two

² The same filling is denoted $\nu_c = 2/5$ in Ref. [17], measured relative to the full filling of the band ($\nu_c = 2$).

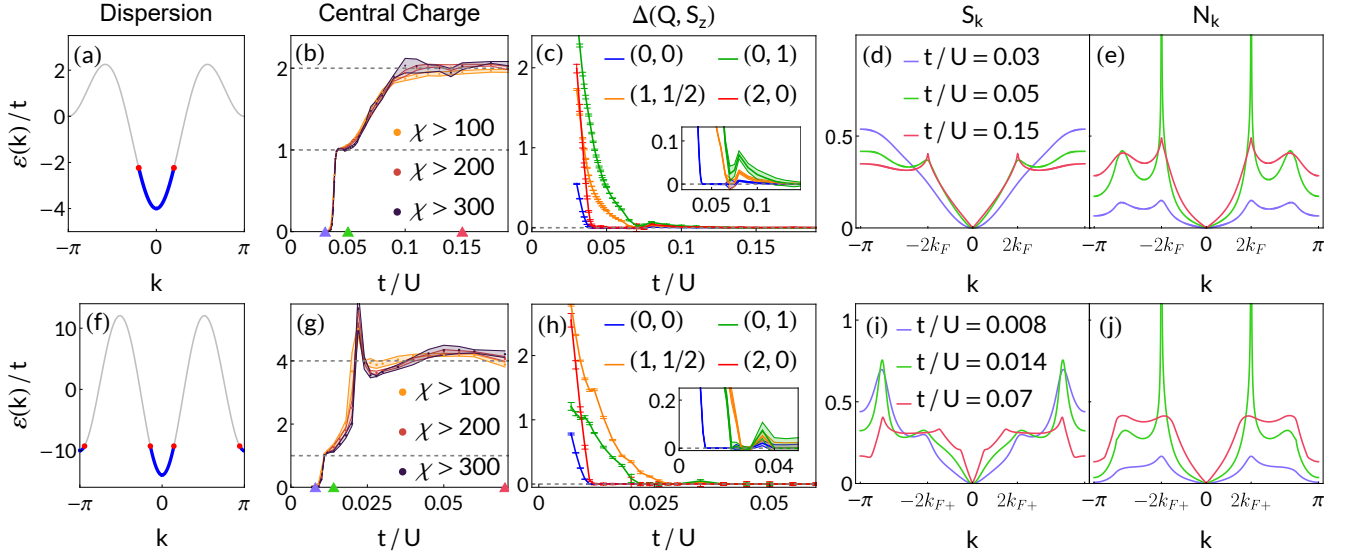


FIG. 2. The two-step WM transition, as shown in Fig. 1a, on the XC2 geometry. Panels (b)-(e) support the scenario $C0S0 \rightarrow C1S0 \rightarrow C1S1$ for the dispersion shown in (a) with 2 Fermi points. Similarly, panels (g)-(h) support the scenario $C0S0 \rightarrow C1S0 \rightarrow C2S2$ for the dispersion shown in (f) with 4 Fermi points. The $C1S0$ phase is a Luther-Emery liquid. Conformal central charge (C) shows a sharp transition from $C = 0$ to $C = 1$ across (b) $t_{c1}/U = 0.04$ (for (a)), and (g) $t_{c1}/U = 0.01$ (for (f)). There is a subsequent gradual increase from (b) $C = 1$ to $C = 2$ across $t_{c2}/U \approx 0.1$ (for (a)), and (g) $C = 1$ to $C = 4$ across $t_{c2}/U \approx 0.024$ (for (f)). Different colors represent C obtained by removing varying number of low- χ states (see main text). (c) and (h) Extrapolated spectral gaps, $\Delta(Q, S_z; \chi)$, in different symmetry sectors across the phase diagram for the dispersions in (a) and (f), respectively. Below t_{c1} all symmetry sectors are gapped; between t_{c1} and t_{c2} the spin sectors remain gapped while the $(Q, S_z) = (0, 0)$ and $(2, 0)$ gaps vanish. For $t > t_{c2}$ all sectors are gapless. (d),(i) Spin and (e),(j) density structure factors for three representative points in the phase diagram (marked by the ‘▲’ in (b) and (g)). In a gapless sector associated with a specific $\{Q, S_z\}$, the corresponding SF $\sim |k|$ for small k and develops singular cusps at $2k_F$, or $2k_{F+} = 2(k_{F1} + k_{F2})$ (see main text).

phases with increasing t . We find that the WM insulator first transitions into an intermediate phase with *gapless* charge excitations but *gapped* spin excitations across t_{c1}/U . This intermediate phase hosts gapless spin-singlet Cooper-pair excitations, even though the electron-like excitations are gapped. With increasing t , there is a subsequent transition at t_{c2}/U where the spin gap closes and we recover the LL. Thus, the melting of the WM insulator fits into the schematic shown in Fig. 1a. For case (a), the WM insulator melting transition follows the sequence $C0S0 \rightarrow C1S0 \rightarrow C1S1$, while for case (b), the sequence is given by $C0S0 \rightarrow C1S0 \rightarrow C2S2$. In both cases, the transition proceeds via an intermediate Luther-Emery liquid ($C1S0$). This is the fluctuating “superconducting” phase, that appears in a purely repulsive model without *any* retardation effects by melting the localized spin-singlet Cooper pairs. We elaborate below on three different diagnostics we use to characterize these two-step transitions.

Let us begin with case (a), where the metallic LL is in the $C1S1$ phase. First, in Fig. 2b, we analyze the evolution of the conformal central charge (C) as a function of t/U . We extract the central charge from the scaling of the entanglement entropy with bond dimension, $S(\chi)$ [38, 40–42]. In the WM phase, the system is fully

gapped and $C = 0$. Across $t_{c1}/U \approx 0.04$, we see a sharp increase in C followed by a plateau around $C \approx 1$. Different colors in Fig. 2b show how the extracted values of C depend on the range of bond dimensions used in the linear regression. As we remove more low- χ states, the plateau becomes more prominent. A central charge of $C = 1$ is consistent with two gapless modes, while the two-component LL phase has four gapless modes. Hence, this plateau is strongly suggestive of a distinct intermediate phase. Across $t_{c2}/U \approx 0.1$, the system enters the LL phase with $C = 2$. The precise location of this latter transition between two gapless phases is difficult to resolve using our current setup, but can in principle be addressed better by using larger χ in a future study.

Second, in Fig. 2c, we clarify the nature of the intermediate phase by studying the evolution of spectral gaps in different symmetry sectors. As our iMPS calculation explicitly conserves total particle number and magnetization, we can label the eigenvalues of the MPS transfer matrix (i.e. the spectrum of correlation lengths) with charge (Q) and spin (S_z) quantum numbers, respectively [43]. The spectrum of iMPS correlation lengths has been shown to be inversely proportional to the energy spectrum of low-lying excitations [44, 45], so one can understand the nature of excitations by studying in-

verse correlation lengths. For our purposes, we define the “spectral gap” in a given symmetry sector, $\Delta(Q, S_z; \chi)$, as the inverse of the largest correlation length in that sector: $\Delta(Q, S_z; \chi) = 1/\xi(Q, S_z; \chi)$.³ It should be understood that this is only truly an energy gap up to a characteristic velocity [44, 45]. In Fig. 2c we plot $\Delta(Q, S_z) = \lim_{\chi \rightarrow \infty} \Delta(Q, S_z; \chi)$ for some of the relevant low-energy symmetry sectors [38]: $(Q, S_z) = (0, 0)$ [blue], $(1, 1/2)$ [orange], $(0, 1)$ [green], and $(2, 0)$ [red]. The WM phase is a fully-gapped phase, and consequently all $\Delta(Q, S_z)$ are non-zero. In the intermediate phase, $\Delta(0, 0)$ and $\Delta(2, 0)$ extrapolate to zero while $\Delta(1, 1/2)$ and $\Delta(0, 1)$ remain finite. This implies that spin sectors are gapped but there are gapless charge excitations, which is consistent with the presence of just two gapless modes in Fig. 2b. Here $\Delta(0, 0)$ represents the gap to a composite (neutral) particle-hole spin-singlet excitation, while $\Delta(2, 0)$ represents a charge- $2e$, spin-singlet (Cooper-pair) excitation. On the other hand, $\Delta(1, 1/2)$ represents the gap for single-electron-like excitations and $\Delta(0, 1)$ is a particle-hole spin-triplet excitation. For larger t/U , we find that these spin gaps vanish around the same point in the phase diagram where the central charge plateaus at $C = 2$, which again is consistent with the interpretation of a transition into the LL phase.

Third, in Figs. 2d and e, we show the density and spin structure-factors (SF) as a function of momentum in the three distinct phases. The spin SF is defined as $\mathcal{S}_k = \frac{1}{5} \sum_{j=1}^5 \sum_l e^{ilk} \langle \mathbf{S}_j \cdot \mathbf{S}_{l+j} \rangle$ where j iterates over the 5-site unit cell and $\mathbf{S}_j = (1/2) \sum_{\alpha, \beta} c_{j, \alpha}^\dagger \boldsymbol{\sigma}_{\alpha, \beta} c_{j, \beta}$. We define the density SF as $\mathcal{N}_k = \frac{1}{5} \sum_{j=1}^5 \sum_l e^{ilk} \langle (n_j - \langle n_j \rangle)(n_{l+j} - \langle n_{l+j} \rangle) \rangle$, subtracting off the average density on each site. This removes any Bragg peaks from \mathcal{N}_k , minimizing the role of spurious translational symmetry breaking at finite χ [38]. In the WM insulator, both the density and spin SF are featureless (non-singular at any k). At small k , they vanish smoothly as $\mathcal{N}_k, \mathcal{S}_k \sim k^2$, indicating a finite spin and charge gap, respectively [46]. In the intermediate phase, the spin SF remains featureless while $\mathcal{N}_k \sim |k|$ for small k , indicating that the charge gap has closed. The density SF also develops singular peaks at $\pm 2k_F$ that appear to diverge in the limit $\chi \rightarrow \infty$. In the LL phase, both the density and spin SF scale as $\mathcal{N}_k, \mathcal{S}_k \sim |k|$ for small k and develop singular cusps at $\pm 2k_F$ [38].

Let us now move to case (b), where the metallic LL is in the $C2S2$ phase. Adopting the same procedure as before to extract the central charge (Fig. 2g), we find that $C = 0$ in the WM phase for $t \leq t_{c1} \approx 0.01U$ and $C = 4$ in the LL phase for $t \geq t_{c2} \approx 0.024U$.⁴ The

peak in the central charge near t_{c2}/U is due to a shifting peak in the spectrum of correlation lengths, which is a common feature when modeling phase transitions using matrix product states [43]. We expect this feature will smooth out as χ is increased. There exists a distinct intermediate gapless phase with $C = 1$ for $t_{c1} \lesssim t \lesssim t_{c2}$. The evolution of the spectral gaps in the different symmetry sectors, (Q, S_z) , also proceeds in an identical fashion, as shown in Fig. 2h.

The results for the spin and charge SF as $C2S2$ evolves into $C0S0$ as a function of decreasing t/U are quite similar to the results for the evolution from $C1S1$ to $C0S0$. The small k behavior for $\mathcal{N}_k, \mathcal{S}_k$ as a function of t/U is similar for case (a) and (b). The singular features at the “ $2k_F$ ” wavevectors require special care, as there are two distinct k_{F1}, k_{F2} associated with the different Fermi points. We find that the intermediate gapless phase exhibits a singular peak at $2(k_{F1} + k_{F2})$ that appears to diverge in the limit $\chi \rightarrow \infty$; there is no singular peak at $2(k_{F1} - k_{F2})$ [38]. This suggests that the evolution from $C2S2$ to $C1S0$ is *not* associated with an umklapp-driven transition, which would open a gap to total charge fluctuations [47]. Instead, both LLs ($C1S1$ and $C2S2$) appear to transition into an intermediate $C1S0$ phase, which is strongly reminiscent of a Luther-Emery liquid [13, 48]. This is further corroborated by the evolution of the Luttinger parameters, K_ρ, K_σ , which we extract from the density and spin SF, respectively [38]. In the intermediate $C1S0$ phase, $K_\rho > 0, K_\sigma \rightarrow 0$, corresponding to gapless charge fluctuations associated with the *total* density.

Five-leg cylinder.— To study the effect of an increasing cylinder width, we perform calculations on the YC5 geometry with isotropic hopping amplitudes. Our results are summarized in Fig. 3. We compute the effective charge (spin) gap by studying the curvature of \mathcal{N}_k (\mathcal{S}_k) near $\mathbf{k} = 0$. To extract, e.g., the charge gap, we take a cross section with the transverse momentum $k_y = 0$ and fit $\mathcal{N}_{(k_x, 0)}$ to the form $(A\Delta_c)(\sqrt{(k_x/\Delta_c)^2 + 1} - 1)$ at small k_x . The parameter Δ_c can then be understood as the effective gap for the charge sector. We find that this technique, which essentially averages over transfer matrix eigenvalues that contribute to the charge and spin sectors, is more amenable to studying complex systems with moderate bond dimensions.

We find evidence of a WM insulating phase for $t/U \lesssim 0.078$ which is well-characterized by the cartoon in Fig. 1(c): spatially-separated pairs of electrons that form spin-singlets. This state is characterized by a spin and charge gap, as shown by the extrapolation (black crosses) in Fig. 3a, featureless spin and charge SFs, and local CDW order (see Fig. 3c). For $t/U \gtrsim 0.095$, we find that both the charge and spin sectors are gapless and the central charge approaches $C = 6$, as expected in the FL phase [38]. In this phase, the spin and charge SFs exhibit more pronounced curvature near $\mathbf{k} = 0$.

³ The MPS correlation length, $\xi_{\text{IMPS}}(\chi)$, is the maximum $\xi(Q, S_z; \chi)$ over all symmetry sectors.

⁴ Note the scales are much smaller in these units because the bandwidth $W \approx 26t$ when $t' = 6t$, whereas $W = 6.25t$ when $t' = t$.

For all χ , the WM insulator melts as t/U is increased; the location at which it melts, however, exhibits a strong χ dependence. Additionally, while the charge gap shows behavior consistent with a direct WM-FL transition, the spin gap displays an extra upturn (e.g. near $t/U = 0.09$ for $\chi = 2400$) that is indicative of more complicated structure – this upturn coincides with a sharp change in the degeneracy of the transfer matrix eigenvalues. These features prevent us from performing a simple extrapolation at fixed t/U , as is standard for MPS analyses.

Intriguingly, however, we find that the gap functions exhibit a scaling collapse when *both* the gap and the value of t/U are rescaled by powers of the bond dimension. This hallmark signature of a quantum critical point allows us to approximate both t_c/U as well as the critical exponents. Specifically, we assume that the gaps take the scaling form $\Delta(t_c - t, \chi) \propto \chi^{\zeta/\delta} f((t_c - t)/\chi^{1/\delta})$ near the transition, which implies that $\Delta(t_c - t) \propto (t_c - t)^\zeta$ as $\chi \rightarrow \infty$. In a field-theoretic setting, the exponent $\zeta = \nu z$, can be naturally expressed in terms of the correlation length (ν) and dynamical exponents (z), respectively, assuming that the transition is truly continuous. We then fit the parameters $\{t_c, \zeta, \delta\}$ for the spin and charge gaps independently, obtaining an approximate location for the transition as well as the critical exponents. The scaling collapses are shown in the inset of Fig. 3 and the scaling forms are shown by the gray dashed lines in Fig. 3a and b. We find that the fits to the spin and charge gaps have slightly different values of t_c , but with overlapping error bars: $t_c^{\text{spin}} = 0.80(1)$ and $t_c^{\text{charge}} = 0.81(1)$. The critical exponents are $(\zeta, \delta)_{\text{spin}} = (0.25(9), -0.9(4))$ and $(\zeta, \delta)_{\text{charge}} = (0.20(8), -0.7(5))$. Fits are performed by defining a cost function in terms of the residuals from an interpolated scaling function, and error bars come from integrating the associated probability distribution [38, 49]. Smaller error bars on $\{t_c, \zeta, \delta\}$ could be obtained by taking more data at intermediate values of χ , but a precise location for the transition would likely require going beyond $\chi = 2400$.

Discussion. – In this letter, we have analyzed the quantum melting of a crystalline Wigner-Mott insulator with well formed spin-singlets into a symmetry-preserving metal using iMPS-based methods. Experiments in moiré TMDs are already well-placed to study such transitions in detail in the future. For two-leg ladders, we find clear evidence for an intermediate gapless Luther-Emery phase, which is distinct from the usual Luttinger liquid. The kinetic energy driven quantum fluctuations thus favor melting the spin-singlets into a fluctuating (spin-gapped) superconductor without a gap to Cooper-pair excitations. We have studied the effect of increasing the spatial extent along the second dimension by analyzing the same problem on five-leg cylinders. There, we find that the intermediate gapless phase vanishes altogether, yielding to a continuous bandwidth-tuned metal-insulator transition. Clearly, the actual evolution of the

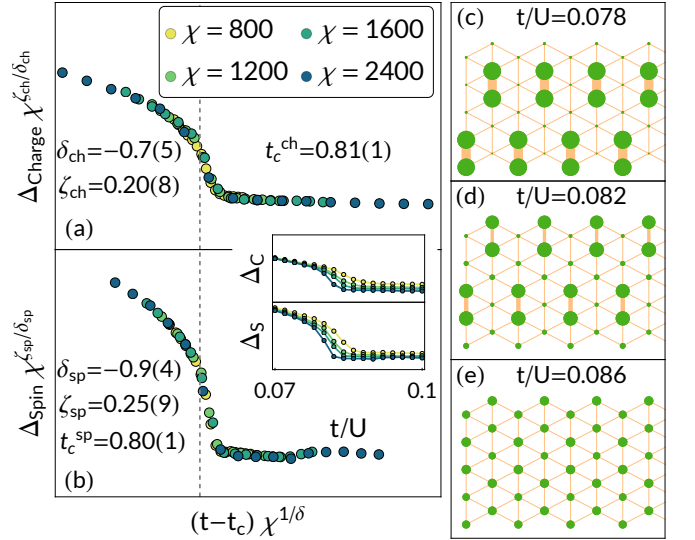


FIG. 3. WM transition on the YC5 geometry. Panels (a) and (b) show the scaling collapse of $\Delta_{c,s}$, extracted from the curvature of the corresponding SF near $\mathbf{k} = 0$ (see main text), in the vicinity of t_c/U . Inset shows the unscaled $\Delta_{c,s}$ versus t/U . For $t/U \lesssim 0.78$ the system has a finite Δ_c , Δ_s , consistent with the WM insulator. Using the scaling collapse, we argue that Δ_c , $\Delta_s \rightarrow 0$ for $t/U \gtrsim 0.82$, consistent with the FL phase. Panels (c)-(e) show real-space pictures of the $\chi = 2400$ state for various t/U , with the green dots proportional to $\sum_{\sigma} \langle n_{i,\sigma} \rangle$ and the thickness of the orange lines denoting the value of $|\langle \mathbf{S}_i \cdot \mathbf{S}_j \rangle|$ between sites. We can see that local spin and charge order vanish at roughly the same point.

many-body ground state as a function of t/U also depends on the $\{V_n\}$. A more exhaustive and systematic computational study of the entire parameter-space as a function of increasing spatial extent along the second dimension and bond dimension will help uncover the energetic considerations leading to the two different scenarios we have highlighted in this paper. Developing complementary analytical methods in two spatial dimensions, going beyond the usual large- N parton-based approaches, to study these transitions is clearly also desirable in light of our findings. It is especially challenging to describe such continuous metal-insulator transitions in the absence of *any* remnant Fermi surface in the insulating state [50, 51], associated with even neutral (e.g. spinon) excitations [52], as observed in our five-leg cylinders. Investigating the effect of inhomogeneities on transport near this metal-insulator transition, building on previous studies at other fillings [53–55] will be of direct experimental interest.

Since there is a strong tendency towards superconductivity near the melting transition associated with the WM insulator, it is natural to address the fate of the ground state with additional doped holes [56, 57]. Given the proximity to charge-ordered states, the resulting superconductor might also be a pair-density wave [58]. The

importance of proximity to the quantum critical point(s), if any, on the associated phenomenology for the doped case also remains an important open question.

Acknowledgements.- DC thanks S. Kim, K.F. Mak, S. Musser, S. Sachdev, T. Senthil, J. Shan and L. Zou for numerous inspiring discussions and collaborations related to continuous metal-insulator transitions. TK thanks E. Mueller for help with the development and implementation of the numerical methods used in this manuscript. We thank S. Musser for clarifying discussions related to the WM transition on the XC2 geometry, and for useful comments on an earlier version of this manuscript. TK is supported by an NSF grant (PHY-2110250). This work is supported in part by a CAREER grant from the NSF to DC (DMR-2237522).

-
- [1] N. Mott, *Metal-Insulator Transitions* (CRC Press, London, 1990).
 - [2] J. M. Luttinger and J. C. Ward, Phys. Rev. **118**, 1417 (1960).
 - [3] M. Oshikawa, Phys. Rev. Lett. **84**, 3370 (2000).
 - [4] M. Imada, A. Fujimori, and Y. Tokura, Rev. Mod. Phys. **70**, 1039 (1998).
 - [5] R. Jamei, S. Kivelson, and B. Spivak, Physical Review Letters **94**, 056805 (2005).
 - [6] A. Camjayi, K. Haule, V. Dobrosavljevic, and G. Kotliar, Nature Physics **4**, 932 (2008).
 - [7] A. Amaricci, A. Camjayi, K. Haule, G. Kotliar, D. Tanaskovic, and V. Dobrosavljevic, Physical Review B **82**, 155102 (2010).
 - [8] D. Vu and S. Das Sarma, Phys. Rev. B **101**, 125113 (2020).
 - [9] S. Musser, T. Senthil, and D. Chowdhury, Phys. Rev. B **106**, 155145 (2022).
 - [10] Y. Xu, X.-C. Wu, M. Ye, Z.-X. Luo, C.-M. Jian, and C. Xu, Phys. Rev. X **12**, 021067 (2022).
 - [11] J. I. Cirac, D. Pérez-García, N. Schuch, and F. Verstraete, Rev. Mod. Phys. **93**, 045003 (2021).
 - [12] U. Schollwöck, Annals of Physics **326**, 96 (2011), january 2011 Special Issue.
 - [13] A. Luther and V. J. Emery, Phys. Rev. Lett. **33**, 589 (1974).
 - [14] E. W. Carlson, V. J. Emery, S. A. Kivelson, and D. Orgad, arXiv e-prints , cond-mat/0206217 (2002), arXiv:cond-mat/0206217 [cond-mat.supr-con].
 - [15] T. Li, S. Jiang, L. Li, Y. Zhang, K. Kang, J. Zhu, K. Watanabe, T. Taniguchi, D. Chowdhury, L. Fu, *et al.*, Nature **597**, 350 (2021).
 - [16] A. Ghiotto, E.-M. Shih, G. S. Pereira, D. A. Rhodes, B. Kim, J. Zang, A. J. Millis, K. Watanabe, T. Taniguchi, J. C. Hone, *et al.*, Nature **597**, 345 (2021).
 - [17] Y. Xu, S. Liu, D. A. Rhodes, K. Watanabe, T. Taniguchi, J. Hone, V. Elser, K. F. Mak, and J. Shan, Nature **587**, 214 (2020).
 - [18] E. C. Regan, D. Wang, C. Jin, M. I. Bakti Utama, B. Gao, X. Wei, S. Zhao, W. Zhao, Z. Zhang, K. Yumigeta, M. Blei, J. D. Carlström, K. Watanabe, T. Taniguchi, S. Tongay, M. Crommie, A. Zettl, and F. Wang, Nature **579**, 359 (2020).
 - [19] X. Huang, T. Wang, S. Miao, C. Wang, Z. Li, Z. Lian, T. Taniguchi, K. Watanabe, S. Okamoto, D. Xiao, S.-F. Shi, and Y.-T. Cui, Nature Physics **17**, 715 (2021).
 - [20] H. W. Jiang, R. L. Willett, H. L. Stormer, D. C. Tsui, L. N. Pfeiffer, and K. W. West, Phys. Rev. Lett. **65**, 633 (1990).
 - [21] J. Yoon, C. C. Li, D. Shahar, D. C. Tsui, and M. Shayegan, Phys. Rev. Lett. **82**, 1744 (1999).
 - [22] M. S. Hossain, M. Ma, K. Rosales, Y. Chung, L. Pfeiffer, K. West, K. Baldwin, and M. Shayegan, Proceedings of the National Academy of Sciences **117**, 32244 (2020).
 - [23] T. Smoleński, P. E. Dolgirev, C. Kuhlenskamp, A. Popert, Y. Shimazaki, P. Back, X. Lu, M. Kroner, K. Watanabe, T. Taniguchi, I. Esterlis, E. Demler, and A. Imamoglu, Nature **595**, 53 (2021).
 - [24] Y. Zhou, J. Sung, E. Brutschea, I. Esterlis, Y. Wang, G. Scuri, R. J. Gelly, H. Heo, T. Taniguchi, K. Watanabe, G. Zaránd, M. D. Lukin, P. Kim, E. Demler, and H. Park, Nature **595**, 48 (2021).
 - [25] H. Li, S. Li, E. C. Regan, D. Wang, W. Zhao, S. Kahn, K. Yumigeta, M. Blei, T. Taniguchi, K. Watanabe, S. Tongay, A. Zettl, M. F. Crommie, and F. Wang, Nature **597**, 650 (2021).
 - [26] M. Roger, Phys. Rev. B **30**, 6432 (1984).
 - [27] S. Chakravarty, S. Kivelson, C. Nayak, and K. Voelker, Philosophical Magazine B **79**, 859 (1999), <https://doi.org/10.1080/13642819908214845>.
 - [28] B. Spivak and S. A. Kivelson, Annals of Physics **321**, 2071 (2006).
 - [29] B. Padhi, R. Chitra, and P. W. Phillips, Phys. Rev. B **103**, 125146 (2021).
 - [30] Y. Zhang, T. Liu, and L. Fu, Phys. Rev. B **103**, 155142 (2021).
 - [31] H. Pan, F. Wu, and S. Das Sarma, Phys. Rev. B **102**, 201104 (2020).
 - [32] H. Pan and S. Das Sarma, Physical Review Letters **127**, 096802 (2021).
 - [33] H. Pan and S. Das Sarma, Phys. Rev. B **105**, 041109 (2022).
 - [34] M. Matty and E.-A. Kim, Nature Communications **13**, 7098 (2022).
 - [35] Y. Zhou, D. N. Sheng, and E.-A. Kim, Phys. Rev. Lett. **128**, 157602 (2022).
 - [36] N. Morales-Durán, A. H. MacDonald, and P. Potasz, Physical Review B **103**, L241110 (2021).
 - [37] N. Morales-Durán, P. Potasz, and A. H. MacDonald, arXiv e-prints , arXiv:2210.15168 (2022), arXiv:2210.15168 [cond-mat.str-el].
 - [38] See supplementary material for additional details related to the effect of long-ranged interactions on the charge-ordering in the wm insulator, a brief description of vumps algorithm and our imp computations, the extrapolation of the spectral gaps, central charge, luttinger parameters, and computation of the structure factors.
 - [39] F. Zauner-Stauber, L. Vanderstraeten, M. T. Fishman, V. Verstraete, and J. Haegeman, Phys. Rev. B **97**, 045145 (2018).
 - [40] F. Pollmann, S. Mukerjee, A. M. Turner, and J. E. Moore, Phys. Rev. Lett. **102**, 255701 (2009).
 - [41] T. G. Kiely and E. J. Mueller, Phys. Rev. B **105**, 134502 (2022).
 - [42] P. Calabrese and J. Cardy, Journal of Statistical Mechanics: Theory and Experiment **2004**, P06002 (2004).

- [43] A. Szasz, J. Motruk, M. P. Zaletel, and J. E. Moore, Phys. Rev. X **10**, 021042 (2020).
- [44] V. Zauner, D. Draxler, L. Vanderstraeten, M. Degroote, J. Haegeman, M. M. Rams, V. Stojevic, N. Schuch, and F. Verstraete, New Journal of Physics **17**, 053002 (2015).
- [45] A. A. Eberharter, L. Vanderstraeten, F. Verstraete, and A. M. Läuchli, Extracting the speed of light from matrix product states (2023).
- [46] R. V. Mishmash, I. González, R. G. Melko, O. I. Motrunich, and M. P. A. Fisher, Phys. Rev. B **91**, 235140 (2015).
- [47] S. Musser and T. Senthil, Phys. Rev. B **106**, 235148 (2022).
- [48] R. Noack, S. White, and D. Scalapino, Physica C: Superconductivity **270**, 281 (1996).
- [49] J. J. Mortensen, K. Kaasbjerg, S. L. Frederiksen, J. K. Nørskov, J. P. Sethna, and K. W. Jacobsen, Phys. Rev. Lett. **95**, 216401 (2005).
- [50] L. Zou and D. Chowdhury, Phys. Rev. Res. **2**, 023344 (2020).
- [51] Y.-H. Zhang and S. Sachdev, Phys. Rev. B **102**, 155124 (2020).
- [52] T. Senthil, Phys. Rev. B **78**, 045109 (2008).
- [53] Y. Tan, P. K. H. Tsang, and V. Dobrosavljević, Nature Communications **13**, 7469 (2022).
- [54] S. Ahn and S. Das Sarma, Phys. Rev. B **105**, 115114 (2022).
- [55] S. Kim, T. Senthil, and D. Chowdhury, Phys. Rev. Lett. **130**, 066301 (2023).
- [56] P. W. Anderson, P. A. Lee, M. Randeria, T. M. Rice, N. Trivedi, and F. C. Zhang, Journal of Physics: Condensed Matter **16**, R755 (2004).
- [57] P. A. Lee, N. Nagaosa, and X.-G. Wen, Rev. Mod. Phys. **78**, 17 (2006).
- [58] D. F. Agterberg, J. S. Davis, S. D. Edkins, E. Fradkin, D. J. Van Harlingen, S. A. Kivelson, P. A. Lee, L. Radzihovsky, J. M. Tranquada, and Y. Wang, Annual Review of Condensed Matter Physics **11**, 231 (2020).
- [59] L. Vanderstraeten, J. Haegeman, and F. Verstraete, SciPost Phys. Lect. Notes, **7** (2019).
- [60] S. R. White, Phys. Rev. B **72**, 180403 (2005).
- [61] I. P. McCulloch, Infinite size density matrix renormalization group, revisited (2008), arXiv:0804.2509 [cond-mat.str-el].
- [62] T. G. Kiely and E. J. Mueller, *manuscript in preparation* (2023).
- [63] J. Osborne, I. P. McCulloch, B. Yang, P. Hauke, and J. C. Halimeh, Large-scale 2 + 1d U(1) gauge theory with dynamical matter in a cold-atom quantum simulator (2022), arXiv:2211.01380 [cond-mat.quant-gas].
- [64] M. M. Rams, P. Czarnik, and L. Cincio, Phys. Rev. X **8**, 041033 (2018).
- [65] B. Vanhecke, J. Haegeman, K. Van Acoleyen, L. Vanderstraeten, and F. Verstraete, Phys. Rev. Lett. **123**, 250604 (2019).
- [66] T. Giamarchi, *Quantum Physics in One Dimension* (Oxford University Press, Oxford, 2003).
- [67] M. Capello, F. Becca, M. Fabrizio, and S. Sorella, Phys. Rev. B **77**, 144517 (2008).

Supplementary Information for “Continuous Wigner-Mott transition at $\nu = 1/5$ ”

Modeling long-range interactions

Electrons in the moiré TMD bilayer experience a long-ranged Coulomb repulsion. By placing two gates parallel to the surface of the bilayer, this interaction can be screened [15–17]. While a variety of gate geometries could be envisioned, here we assume the common scenario of two gates equally spaced away from the moiré bilayer by a distance $d/2$. This leads to the screened potential [17]

$$V(r) = \frac{e^2}{4\pi\epsilon\epsilon_0} \sum_{k=-\infty}^{\infty} \frac{(-1)^k}{\sqrt{r^2 + (kd)^2}}. \quad (2)$$

For both the XC2 and YC5 geometries, we choose the experimentally-relevant value $d/a = 10$ where a is the moiré lattice spacing.

In general, non-exponential interactions cannot be efficiently represented as a matrix product operator, meaning that iMPS simulations require some form of truncation. This leaves the additional question of where we truncate the interactions. This can be a common problem in quasi-two-dimensional geometries, as the shorter cylindrical direction will often stabilize symmetry-broken states that are unstable in the thermodynamic limit.

In Fig. S1, we plot the classical energy (i.e. in the limit $t/U, t/V_1 \rightarrow 0$) of the two low-energy charge configurations, pictured as insets, as a function of d/a . The upper two plots show the energy when we keep up to third-nearest-neighbor interactions, and the lower two plots show the energy when keeping up to fourth-nearest-neighbor interactions.

For the XC2 geometry, we find that the “zig-zag” ground state (blue) always has a lower energy than the “aligned-pairs” state (green). Moreover, due to the constrained geometry, both of these states can lower their respective energies via superexchange when $t/U > 0$. For the YC5 geometry, we find that third-nearest-neighbor interactions lead to a crossover as a function of d/a : for $d/a \lesssim 3$, the aligned-pairs state (blue) has a lower energy, while above that value the zig-zag state (green) is the classical ground state. For the YC5 geometry, this latter state can be thought of as spatially-separated antiferromagnetic Heisenberg chains. The crossover behavior is not desirable, as the introduction of superexchange at finite t/U could lead to a transition between these charge-ordered states.

Inclusion of the fourth-nearest-neighbor interaction removes this ambiguity in favor of the aligned-pairs ground state, which agrees with classical Monte Carlo simulations of the full 2D model [17]. Hence, for consistency, we include up to fourth-nearest-neighbor interactions on both the XC2 and YC5 geometries.

Description of VUMPS

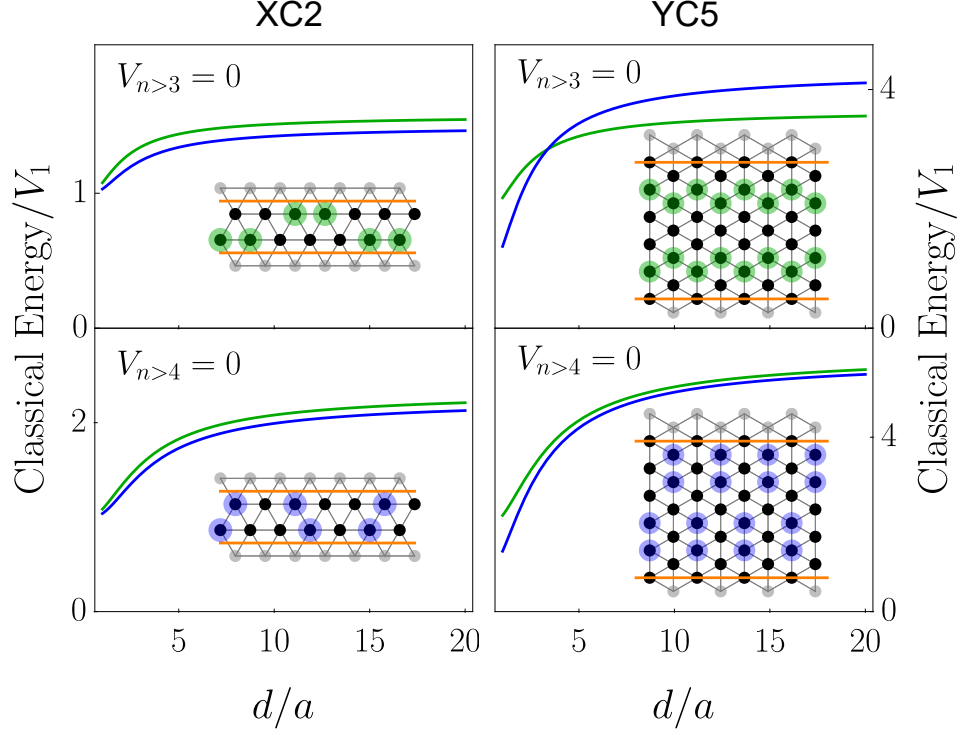
In this section we provide a brief introduction to the variational uniform matrix product states (VUMPS) algorithm, which was developed in Ref. [39]. For a more extended discussion of the algorithm and notation, we refer interested readers to Refs. [39, 41, 59].

A finite MPS on an L -site lattice can be represented as

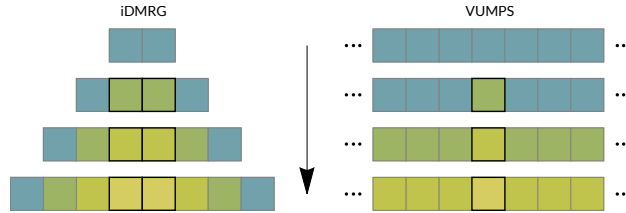
$$|\psi\rangle = \sum_{\sigma} A_1^{\sigma_1} A_2^{\sigma_2} \cdots A_L^{\sigma_L} |\sigma_1 \sigma_2 \cdots \sigma_L\rangle \quad (3)$$

where the $A_i^{\sigma_i} \equiv [\mathbf{A}_i]_{s_i, s_{i+1}}^{\sigma_i}$ are rank-3 tensors that exist on physical lattice sites, enumerated by the index i . The variable σ_i is taken here to represent the single-site Hilbert space of the model – for the Fermi-Hubbard system we study here, this Hilbert space is spanned by the states $\{|\emptyset\rangle, |\uparrow\rangle, |\downarrow\rangle, |\uparrow\downarrow\rangle\}$. The state $|\sigma_1 \sigma_2 \cdots \sigma_L\rangle$ is understood to be a product state over the length- L system. In this way, Eq. (3) represents an MPS as a superposition of all possible product states. The coefficients of each product state is found by contracting the matrices $A_1^{\sigma_1} A_2^{\sigma_2} \cdots A_L^{\sigma_L}$ over the virtual indices s_i . The dimensions of these virtual indices are known as the “bond dimensions” of the system. In the limit that the bond dimension is taken to infinity, Eq. (3) can represent any wavefunction on a length- L lattice.

The iMPS is merely the extension of Eq. (3) to the limit $L \rightarrow \infty$. In order to do this, we have to make a choice that the wavefunction is periodic with a unit cell of length n . When contracting the iMPS, there is no longer an explicit open boundary condition. This changes what it means to take expectation values or overlaps with respect to the iMPS: rather than sequentially contracting tensors from the left or right boundary, one must consider the asymptotic



Supplemental Figure S1. Classical energy ($t/U, t/V_1 \rightarrow 0$) per unit cell of the two low-energy charge configurations for XC2 and YC5 geometries as a function of gate separation, d/a , for two possible truncations. For both XC2 and YC5, blue and green curves correspond to the blue and green charge configurations, shown as real-space cartoons in the insets.



Supplemental Figure S2. Cartoon representing the distinction between the iDMRG and VUMPS algorithms, reproduced from Ref. [41]. Individual squares represent the particular rank-2 or rank-3 tensors comprising an MPS. For each method, the wavefunction from the previous iteration serves as a “bath” from which the next optimal state is chosen. While iDMRG grows a finite chain outwards by adding tensors in the center, VUMPS performs global updates after each iteration and enforces that the state be translationally-invariant.

behavior of the iMPS transfer matrix. For a comprehensive discussion of the properties of infinite MPS, we refer the reader to Ref. [59].

Given this brief introduction, we can now understand the nature of the VUMPS algorithm by contrasting it with the standard way of determining ground states in the thermodynamic limit: the infinite density matrix renormalization group (iDMRG) [12, 60, 61]. The iDMRG algorithm consists of an initial finite-size MPS comprising two unit cells. One then “grows” the initial state by adding two additional unit cells to the center of the chain and solving an eigenvalue problem to determine their lowest-energy configuration. Note that this step only modifies the additional two unit cells – the boundary tensors remain fixed. This process is then repeated until the unit cells being added to the center have converged to a fixed point. This algorithm is illustrated pictorially on the left side of Fig. S2. One can then construct an iMPS out of those unit cells, which should be the ground state in the thermodynamic limit.

The VUMPS algorithm explicitly considers an iMPS at each stage of the optimization. Starting with an initial iMPS, one computes the action of the Hamiltonian on that state by computing the left and right fixed points of the MPO transfer matrix [39, 59]. Given these fixed points, one constructs an effective Hamiltonian that acts on each

individual tensor of the iMPS. Using one of two methods [39], one then updates each tensor in the unit cell and constructs a new iMPS out of the updated tensors. This is illustrated on the right half of Fig. S2. The process is then repeated until the variational gradient (i.e. the gradient of the variational energy with respect to the variational parameters) is reduced below a desired level. A vanishing gradient implies both that the state is truly uniform and that the wavefunction is variationally optimal. It was shown in Ref. [39] that the ground states obtained by iDMRG can have variational gradients as large as $\sim 10^{-4}$, while VUMPS can attain considerably lower gradients.

Details of the iMPS calculations

In our calculation, we compute the ground state at a given bond dimension using the VUMPS algorithm with single-site series-style updates [39]. For the XC2 geometry, we use a five-site unit cell; for the YC5 geometry, we use a ten-site unit cell. In both cases, we verify that increasing the unit cell has no effect on physical observables. At a particular bond dimension (defined as the maximum over all possible bond dimensions across the unit cell), we perform single-site VUMPS updates until the gradient has been reduced below 10^{-7} .

As discussed in the main text, our simulations conserve both the total particle number and total magnetization of the system. An important problem in the application of VUMPS is that the algorithm was developed with a single-site update, which does not allow one to grow the bond dimension. Furthermore, when using block-sparse (symmetry-conserving) tensors, the bond dimension must be grown carefully to ensure that relative block sizes are optimally chosen. Ref. [39] proposes a way of doing this via a subspace expansion, which has the benefit of preserving translational invariance in the state. For the XC2 geometry, we expand the bond dimension using this technique. For the YC5 geometry, however, we found the use of successive expansions and single-site optimizations to be cumbersome given the larger bond dimensions. For that reason, we employed an alternative integration of the time dependent variational principle (iTDVP) equations, sweeping from left to right using infinite boundary conditions. This is more natural when working with larger unit cells and can easily be extended to two-site updates, as is necessary to optimally increase the bond dimension. The technique will be described in detail in a forthcoming paper [62] and is similar in spirit to that used in Ref. [63].

Spectral gap extrapolation

As noted in the main text, the spectrum of the iMPS transfer matrix contains all information about correlation functions in the system. In particular, any two-point correlation function can be written in the eigenbasis of the MPS transfer matrix, i.e.

$$\begin{aligned} \langle A_i B_j \rangle &= (\mathcal{J}_i(A), (\mathcal{T}^{i-j-1}, \mathcal{J}_j(B))) \\ &= \sum_{n=0}^{\chi^2-1} (\mathcal{J}_i(A), \nu_n^R) \lambda_n^{i-j-1} (\nu_n^L, \mathcal{J}_j(B)) \end{aligned} \quad (4)$$

where $\nu_n^{L,R}$ are the left and right eigenvectors of the transfer matrix, λ_n is the associated eigenvalue, \mathcal{J} are the “form factors” associated with the operators A and B , and (\dots, \dots) is an inner product with respect to the virtual degrees of freedom (i.e. the bond dimension) [44]. Note in particular that the only term depending on the separation $|i - j|$ is λ_n^{i-j-1} . In that sense, the spectrum of the transfer matrix defines a set of correlation lengths out of which every two-point correlation function is composed.

Normalization of the wavefunction requires that the largest eigenvalue, λ_0 , be equal to 1. Hence, the correlation length of the iMPS, ξ_{iMPS} , is defined in terms of the magnitude of the second-largest transfer matrix eigenvalue:

$$\xi_{\text{iMPS}} \equiv -1/\ln |\lambda_1/\lambda_0| = -1/\ln |\lambda_1|. \quad (5)$$

By definition, this is the longest possible correlation length of any correlation function computed with respect to the iMPS.

As suggested by the analysis of Ref. [44], one can map the dominant eigenvalues of the transfer matrix to the low-energy spectrum of the model being studied. The justification for this is that a system with a gap Δ will have a finite correlation length $\xi \sim 1/\Delta$ [40, 44]. Of course, this mapping only holds up to an overall scale factor. For this reason, we do not concern ourselves with the absolute magnitude of these correlation lengths; rather, we focus on

their relative sizes and whether they scale to zero. In particular, when modeling a gapless phase, a given iMPS will always display a gap but $\lim_{\chi \rightarrow \infty} \xi_{\text{iMPS}}(\chi) = 0$.

We can learn even more about the state by considering the largest transfer matrix eigenvalues in different symmetry sectors. For example, if one were to compute the single-particle density matrix, $\langle c_{i,\uparrow}^\dagger c_{j,\uparrow} \rangle$, the form factors encode the fact the total particle number and total spin changed on site i and changed back on site j . As we are conserving both particle number and spin, that means the eigenvectors ν_n that overlap with those form factors are in the sector $(Q, S_z) = (1, 1/2)$, where Q denotes the charge (particle number) and S_z denotes the \hat{z} magnetization. By contrast, the operator $n_{i,\uparrow}$ does not change the quantum numbers of the wavefunction, and hence the correlation function $\langle n_{i,\uparrow} n_{j,\uparrow} \rangle$ is propagated by eigenvectors in the $(Q, S_z) = (0, 0)$ sector.

In order to reliably extrapolate the transfer matrix eigenvalues in the limit $\chi \rightarrow \infty$, we adopt the procedure of Ref. [64]. We define a refinement parameter $\delta = \Delta_1 - \Delta_0$ where $\Delta_0 = 1/\xi_{\text{iMPS}}$ and Δ_1 is the next smallest inverse correlation length. In the limit $\chi \rightarrow \infty$, δ should vanish whether one is in a gapped or a gapless phase (up to degeneracies, see generalizations in Ref. [65]). Hence, one can reliably extrapolate the transfer matrix eigenvalues to their asymptotic values by studying how they scale in the limit $\delta \rightarrow 0$. We find that this procedure yields results consistent with a direct $1/\chi \rightarrow 0$ extrapolation, but it reduces noise.

Central charge

When a conformally-invariant one-dimensional system is confined to a length- L system, the entanglement entropy of a bipartition of the system scales as $S = \frac{C}{6} \ln(L)$ where C is the conformal central charge [42]. Although an iMPS is formally infinite, it has been established [40, 41] that its finite correlation length can be treated in a manner similar to a length cutoff. Hence, one finds that the entanglement entropy of the variational wavefunction scales as $S(\chi) = \frac{C}{6} \ln(\xi_{\text{iMPS}}(\chi))$. We are able to independently compute the entanglement entropy and iMPS correlation length for each bond dimension, and hence can extract the conformal central charge via a linear regression.

For the XC2 geometry, the expected central charge of a $C\alpha S\beta$ phase (which has α gapless charge modes and β gapless spin modes) is $\alpha + \beta$. For the YC5 geometry, momentum modes along the transverse direction are quantized by the periodic geometry. The expected central charge can be found from the number of times that these momentum cuts intersect the isotropic Fermi surface [43]. As shown in Fig. 1c, the $\nu = 1/5$ Fermi surface is intersected by 3 momentum cuts, yielding an expected central charge of $C = 6$.

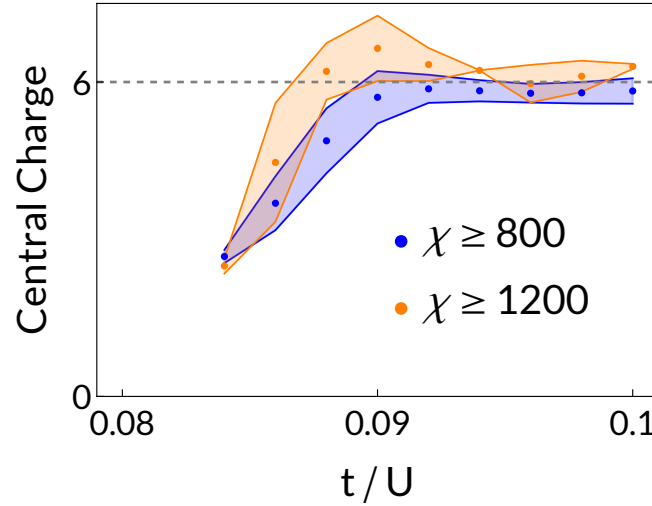
For the YC5 geometry, the presence of the intermediate region prevents us from performing the simple fit $S(\chi) = \frac{C}{6} \ln(\xi_{\text{iMPS}}(\chi))$ to extract C . This can be attributed to the upturn in the spin gap in the $\chi = 1600$ and 2400 datasets (Fig. 3), resulting in non-monotonic behavior (the associated correlation length ξ_{iMPS} exhibits an analogous upturn). Notably, however, the charge gap appears insensitive to this intermediate behavior. Moreover, the charge gap, which should be viewed as a sort of “average” over all correlation lengths contributing to the density-density correlation function, is less than or equal to the spin gap at all points in Fig. 3. Hence, we identify a correlation length $\xi_{\text{Charge}} = 1/\Delta_{\text{Charge}}$ and study the scaling behavior of this quantity as a function of bond dimension. As argued in Refs. [40, 41], the iMPS correlation length in a gapless phase with conformal central charge C scales as $\xi_{\text{iMPS}} \propto \chi^{-\kappa}$ where $\kappa = \frac{6/C}{\sqrt{12/C+1}}$. Importantly, all vanishing correlation lengths should display the same exponent, so the substitution $\xi_{\text{iMPS}} \rightarrow \xi_{\text{Charge}}$ should not affect the value of κ . We utilize this scaling relation, rather than $S(\chi) = \frac{C}{6} \ln(\xi_{\text{iMPS}}(\chi))$, as this removes all dependence on the spin variables. As shown in Fig. S3, the central charge extracted from the charge gap plateaus in the vicinity of $C \approx 6$, the expected value in the FL phase, for $t/U \gtrsim 0.09$.

Luttinger parameters

In one-dimensional systems, the long-wavelength behaviors of \mathcal{N}_k and \mathcal{S}_k are related to the charge and spin Luttinger parameters, respectively [66]. Specifically, following the definitions proposed in Ref. [46] for spin-1/2 fermions on an XC2 geometry, we have

$$\mathcal{N}_k = \frac{2K_\rho}{\pi} |k| + \mathcal{O}(k^2), \quad (6)$$

$$\mathcal{S}_k = \frac{3K_\sigma}{2\pi} |k| + \mathcal{O}(k^2). \quad (7)$$



Supplemental Figure S3. Plot of the conformal central charge in the vicinity of the FL phase on the YC5 cylinder, extracted by fitting $\xi_{\text{Charge}} \propto \chi^{-\kappa}$ where $\kappa = \frac{6/C}{\sqrt{12/C+1}}$ [40, 41]. Different curves use different low- χ cutoffs. The central charge appears to increase until around $t/U \approx 0.09$, beyond which it plateaus around $C = 6$ (dashed line). This is the expected value of the central charge in the FL phase.

These definitions are formulated to capture the behavior of the two-component Luttinger liquid phase, and in particular they satisfy the non-interacting relation in which $K_\rho = K_\sigma = 1$ and $\mathcal{S}_k = \frac{3}{4}\mathcal{N}_k$. Notably, when applied to the 4-Fermi-point case, these definitions yield Luttinger parameters for the *total* spin and charge modes, respectively [46, 47].

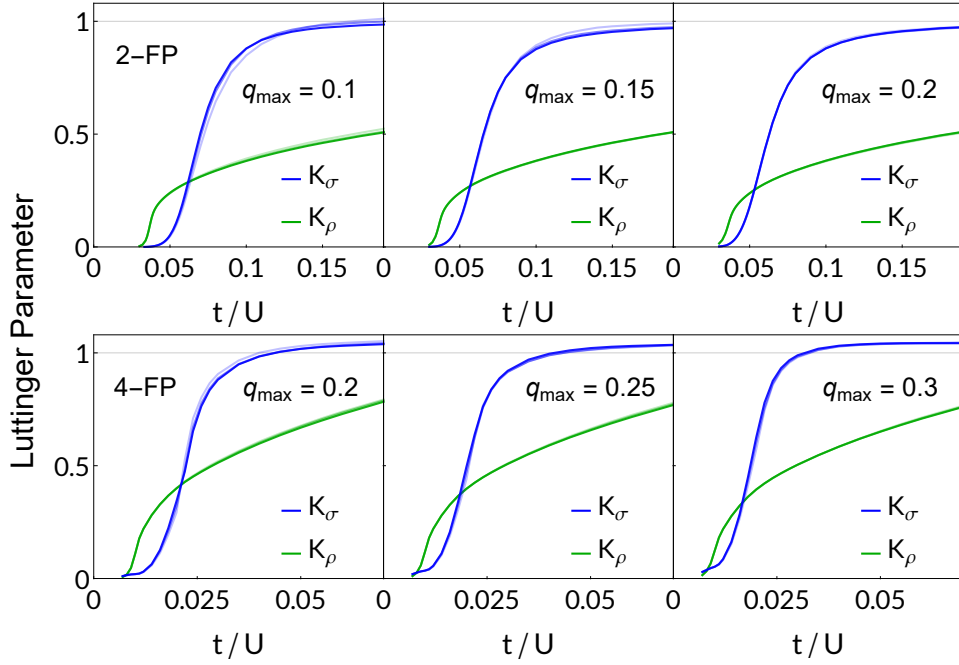
As an iMPS is a gapped ansatz, it will never formally satisfy the above relationships – instead, a gapped state will have leading-order contributions $\text{SF}(k) \propto k^2$ [67]. In gapless phases, however, Eqs. (6) and (7) will emerge as χ is increased and ξ_{iMPS} vanishes. Hence, when extracting approximate Luttinger parameters numerically, it is important to keep two scales in mind: (1) Generically Eqs. (6) and (7) are only satisfied below some cutoff momentum $q_{\text{cut}}^{\mathcal{N},\mathcal{S}}(t/U)$ that vanishes in the vicinity of t_{c1} (for \mathcal{N}_k) or t_{c2} (for \mathcal{S}_k); (2) Even when Eqs. (6) and (7) hold, the correlation function of an iMPS with bond dimension χ will only faithfully represent this behavior down to momenta $q_{\text{iMPS}}^{\mathcal{N},\mathcal{S}}(\chi, t/U) \sim 1/\xi_{\text{iMPS}}(\chi, t/U)$. Thus, resolving the spin and charge Luttinger parameters requires one to identify the smallest range of momenta that are faithfully represented in the iMPS correlation functions. The behavior of the Luttinger parameters in the vicinity of critical points is often rounded off, as this is a place where $q_{\text{cut}}^{\mathcal{N},\mathcal{S}} \rightarrow 0$. This behavior can be ameliorated, but never completely removed, by further increasing the bond dimension.

In Fig. S4 we represent this tradeoff by showing the spin and charge Luttinger parameters across the phase diagram resulting from fits of the form $A_\mu|k| + B_\mu k^2$ ($\mu = \rho, \sigma$) to \mathcal{N}_k and \mathcal{S}_k , respectively. Each panel uses only momenta $|k| \leq q_{\text{max}}$ for the fit, where $q_{\text{max}} = 0.1, 0.15$ and 0.2 for the 2FP data set and $0.2, 0.25$ and 0.3 for the 4FP data set. Each line denotes coefficients for different bond dimensions, where the more opaque curves have a larger bond dimension. We find that K_ρ increases sharply around t_{c1} and then smoothly increases as a function of t/U . K_σ , by contrast, remains essentially zero through t_{c1} and then gradually increases, plateauing at $K_\sigma \approx 1$ around t_{c2} . This very gradual increase as a function of t/U is expected because this latter phase transition takes place between two gapless phases [43]. The final value $K_\sigma = 1$ arises in any gapless phase with $\text{SU}(2)$ spin symmetry [66], and hence is consistent with our expectations in the two-component Luttinger liquid phase.

Structure factors

When computing the density structure factor, \mathcal{N}_k , we explicitly subtract off the average values of the density on respective sites. That is, the density SF is defined as

$$\mathcal{N}_k = \frac{1}{5N^*} \sum_{j=1}^5 \sum_{l=-N^*}^{N^*} e^{ilk} \langle (n_j - \langle n_j \rangle) (n_{l+j} - \langle n_{l+j} \rangle) \rangle \quad (8)$$



Supplemental Figure S4. Plot of the Luttinger parameters K_ρ and K_σ extracted via a fit of the form $A_\mu|k| + B_\mu k^2$ to the structure factors \mathcal{N}_k and \mathcal{S}_k for small k . Top row are results for the 2-Fermi-point calculation and bottom row are for the 4-Fermi-point results. We constrain the fit to values of $|k| \leq q_{\max}$, with q_{\max} labeled on each plot. Different curves correspond to different bond dimensions, with more opaque curves corresponding to a larger χ .

where N^* is the maximum displacement included (for the plots in the main text, $N^* = 10000$). The reason for this subtraction is to remove spurious features of the gapless states: we find that all states across the phase diagram exhibit translational symmetry breaking of some form, but this vanishes asymptotically in the gapless phases.

There are no such Bragg peak contributions to the spin structure factor, so we simply define it as

$$\mathcal{S}_k = \frac{1}{5N^*} \sum_{j=1}^5 \sum_{l=-N^*}^{N^*} e^{ilk} \langle \mathbf{S}_j \cdot \mathbf{S}_{l+j} \rangle \quad (9)$$

where the spin operators are given by $\mathbf{S}_j = (1/2) \sum_{\alpha,\beta} c_{j,\alpha}^\dagger \boldsymbol{\sigma}_{\alpha,\beta} c_{j,\beta}$.

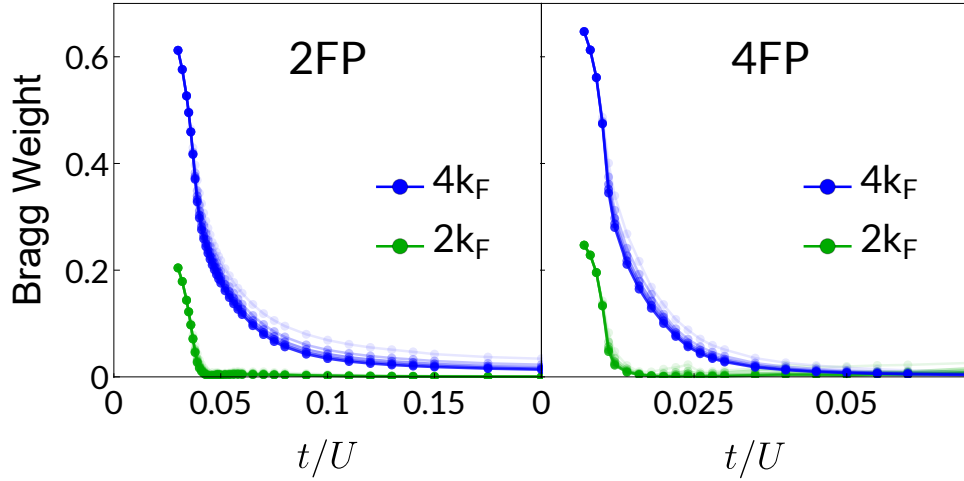
We can study the evolution of these Bragg peak contributions independently by Fourier transforming the density profile $\bar{n}_i \equiv \langle n_i \rangle$. As we use a five-site unit cell when studying the XC2 geometry, reflection symmetry dictates that there are 3 non-trivial “Bragg peak” contributions: $\bar{n}_{k=0}$, $\bar{n}_{k=\pm 2k_F}$, and $\bar{n}_{k=\pm 4k_F}$. The $k = 0$ component is simply the average density per site, and hence remains fixed throughout the phase diagram. The finite- k components, by contrast, are not fixed – a finite value of these peaks corresponds to long-range charge order at the associated wavevectors.

In Fig. S5 we plot the “Bragg weight”, which we define as $|\bar{n}_k|$, at the two finite wavevectors across the phase diagram. We present the data for a variety of bond dimensions $100 \leq \chi \leq 500$, where more opaque points correspond to larger bond dimensions. For both the 2-Fermi-point and 4-Fermi-point systems, the intermediate phase corresponds to a vanishing $2k_F$ Bragg peak and a persistent $4k_F$ peak.

As noted in the main text, we use the lack of incommensurate peaks in the 4-Fermi-point \mathcal{N}_k as an indication that the *total* charge mode remains gapless in the intermediate phase, rather than the relative charge mode [47]. These singularities can be difficult to identify from Fig. 2 directly, so in Fig. S6 we plot the derivative $d\mathcal{N}_k/dk$ for the same three points in the phase diagram.

Of note is the fact that the 2-FP and 4-FP data are indistinguishable in the WM and intermediate phases, while in the metallic phase the 4-FP data has considerably more structure. These additional peaks occur at other (incommensurate) momenta for which 2-particle scattering events can occur between any of the 4 Fermi points.

Additionally, to support our claims that $\text{SF} \sim |k|$ in phases where the associated sector is gapless, in Fig. S7 we show a zoom-in to small- k for the structure factors shown in Figs. 2 and S6. Colors are defined to be consistent with the previous graphs. While an MPS can never have proper $\text{SF} \sim |k|$ behavior, we see that the gapless phases exhibit



Supplemental Figure S5. Bragg weights as a function of t/U for the 2-Fermi-point (2FP) and 4-Fermi-point (4FP) systems. Results for finite- χ are shown, with more opaque data corresponding to larger bond dimensions. In both cases, we find that the $2k_F$ Bragg peaks vanish continuously at t_{c1} while the $4k_F$ peaks persist until t_{c2} .

approximately linear behavior up to a certain momentum scale, below which it crosses over to quadratic behavior. In particular, note that the red S_k curves exhibit this feature for both the 2FP and 4FP data, while the green S_k curves show pronounced quadratic behavior. This is indicative of the spin gap in the Luther-Emery liquid phase. By contrast, both the green and red \mathcal{N}_k curves are linear for the 2FP and 4FP data points.

On the YC5 cylinder, we compute structure factors in an analogous way:

$$\mathcal{N}_k = \frac{1}{10} \sum_{j=1}^{10} \sum_{\mathbf{r}} e^{i\mathbf{k} \cdot \mathbf{r}} \langle (n_{\mathbf{r}_j} - \langle n_{\mathbf{r}_j} \rangle) (n_{\mathbf{r}_j + \mathbf{r}} - \langle n_{\mathbf{r}_j + \mathbf{r}} \rangle) \rangle \quad (10)$$

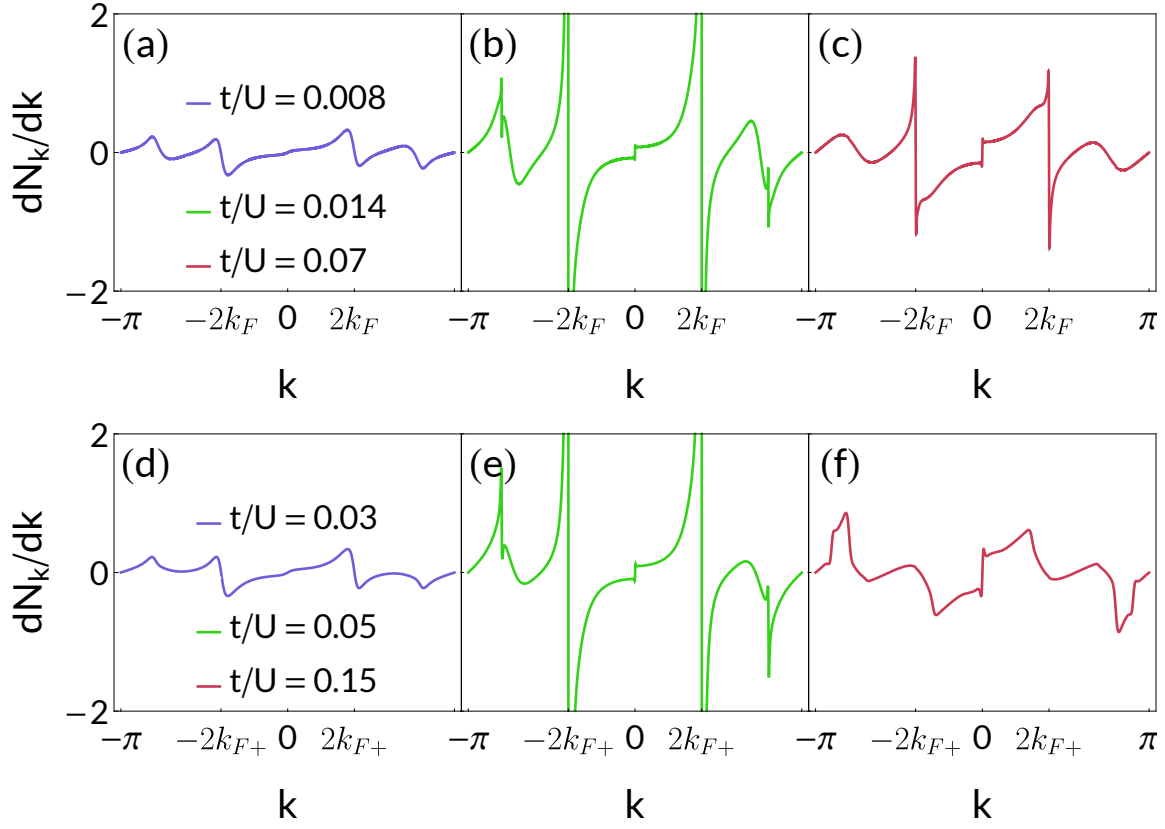
$$S_k = \frac{1}{10} \sum_{j=1}^{10} \sum_{\mathbf{r}} e^{i\mathbf{k} \cdot \mathbf{r}} \langle \mathbf{S}_{\mathbf{r}_j} \cdot \mathbf{S}_{\mathbf{r}_j + \mathbf{r}} \rangle \quad (11)$$

The sums over j sum over the sites in the unit cell, and \mathbf{r}_j is the two-dimensional position of site j . We define the \hat{y} direction as the short one (along the circumference of the cylinder). The data used for the scaling collapse in Fig. 3 comes from fitting the $k_y = 0$ cross section to the form $A\Delta\sqrt{(k_x/\Delta)^2 + 1} - 1$, which interpolates between $\sim k_x^2$ and $\sim |k_x|$ behavior as $\Delta \rightarrow 0$. Representative cross sections are shown in Fig. S8.

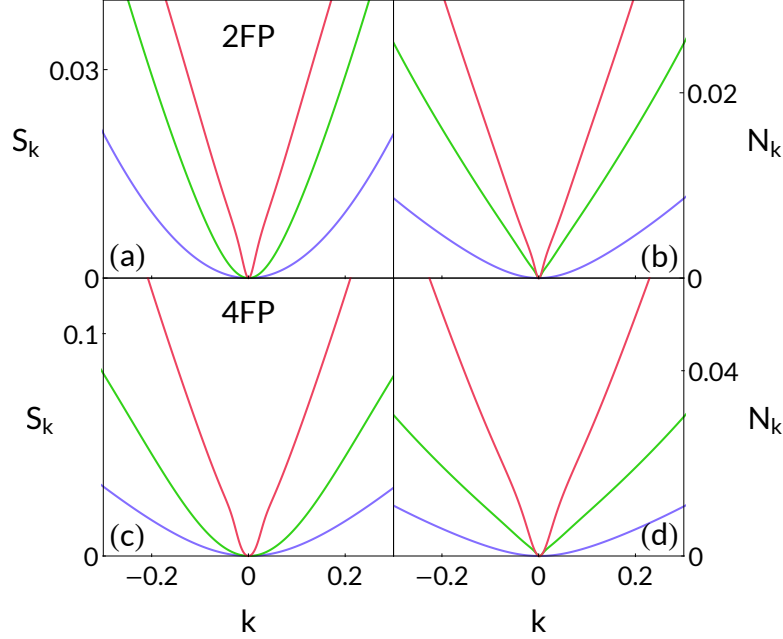
Scaling Collapse

The scaling collapse parameters are computed numerically by interpolating each rescaled dataset at fixed bond dimension and computing residuals of all other datasets from the interpolated curves. For the YC5 data in Fig. 3, we use only data with $\chi \geq 800$. Error bars are estimated by defining a “thermal” probability distribution according to Ref. [49]. We then integrate the probability distribution along the axis associated with the desired fitting parameter, producing a cumulative distribution function (CDF) for that parameter. The width of this CDF defines the error bars for our parameters.

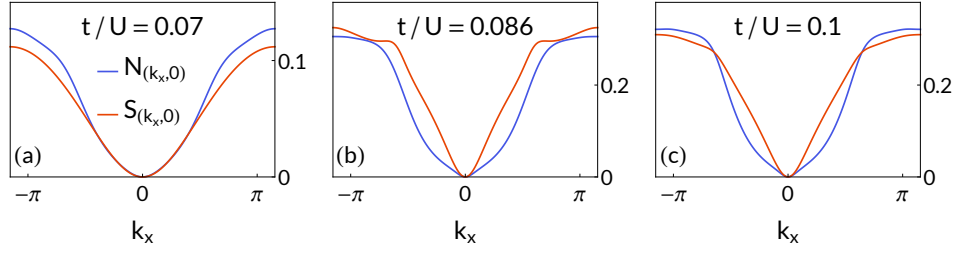
The rescaling procedure applied to the YC5 data can readily be applied to other quantum critical points. To demonstrate this, we replicate the YC5 analysis on the 2-Fermi-point XC2 data used in Fig. 2. Here we’ll search for a scaling collapse in the transfer matrix eigenvalues $\Delta(Q, S_z)$, which are extrapolated in Fig. 2c. In Fig. S9a we plot the rescaled $\Delta(0, 0)$, which extrapolates to zero at t_{c1} as shown in Fig. 2. We assume the scaling form $\Delta(0, 0; \chi) \propto (t_{c1} - t)^{\zeta_1/\delta_1} f((t_{c1} - t)/\chi^{1/\delta_1})$ near the transition, and we extract the fit parameters $\{t_{c1}, \zeta_1, \delta_1\}$ by minimizing the residuals from an interpolated scaling function. We find that $(t_{c1}, \zeta_1, \delta_1) = (0.0397(3), 0.52(2), -2.15(5))$, which are consistent with the value of t_{c1} found by direct extrapolation. Fig. S9b shows the analogous calculation for the single-particle gap, $\Delta(1, 1/2)$. There we find a scaling collapse with fitted parameters $(t_{c2}, \zeta_2, \delta_2) = (0.10(1), 5.9(1), -7.7(2))$. Again, these are consistent with the direct-extrapolation procedure.



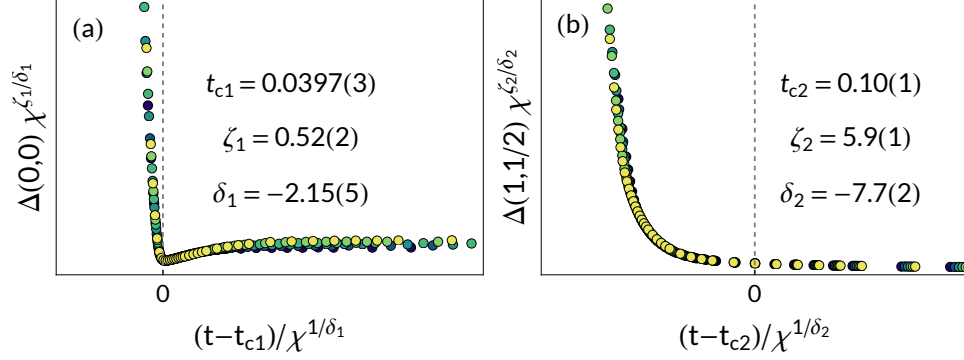
Supplemental Figure S6. Derivatives dN_k/dk for the density SFs shown in Fig. 2. Panels (a)-(c) correspond to the 2-Fermi-point data while panels (d)-(f) correspond to 4-Fermi-point data. Notably, while the rightmost panel shows structure in N_k at a variety of incommensurate wavevectors, the intermediate phase shows peaks only at $2k_{F+}$ and $4k_{F+}$. This indicates that the total charge mode remains gapless.



Supplemental Figure S7. Zoom in on the representative SFs (shown in Figs. 2 and S6, with colors defined accordingly) near $k = 0$. This shows more clearly the linear vs. quadratic distinction, elucidating the structures that were noted in the main text.



Supplemental Figure S8. Representative plot of cross-sections of the spin and charge SFs across the YC5 phase diagram. These SFs are computed from the $\chi = 2400$ wavefunctions.



Supplemental Figure S9. (a) Scaling collapse of the transfer matrix eigenvalue $\Delta(0,0)$, defined in the main text, for the 2-Fermi-point data on the XC2 lattice. We find a value of t_{c1} that is in close agreement with the extrapolated value from the main text. (b) The same procedure produces a scaling collapse of the single-particle gap, $\Delta(1,1/2)$, at a value $t_{c2} \approx 0.1$. While the error bars are larger for this fit, again these results are consistent with those found from extrapolation in Fig. 2.